Chinese Chemical Letters 35 (2024) 108812

Contents lists available at ScienceDirect

Chinese Chemical Letters

journal homepage: www.elsevier.com/locate/cclet

Electron-microscopical visualization on the interfacial and crystallographic structures of lithium metal anode

Jiale Zheng[a], Mei Chen[b], Huadong Yuan[a,*], Jianmin Luo[a], Yao Wang[a], Jianwei Nai[a], Xinyong Tao[a,*], Yujing Liu[a,*]

[a] College of Materials Science and Engineering, Zhejiang University of Technology, Hangzhou 310014, China
[b] College of Mechanical and Energy Engineering, Zhejiang University of Science and Technology, Hangzhou 310014, China

ARTICLE INFO

Article history:
Received 8 May 2023
Revised 27 May 2023
Accepted 12 July 2023
Available online 16 July 2023

Keywords:
Li metal anode
Electron microscopy
Visualization
High-resolution
Battery

ABSTRACT

Lithium (Li) metal anodes (LMAs) have garnered significant attention as a potential solution for developing high-energy density batteries, given their theoretical specific capacity and redox potential. However, safety concerns and internal cycling stability issues originated from uncontrollable Li dendrite growth have impeded the practical application of LMAs. Probing the interface between Li metal and electrolyte is a crucial process that offers valuable insights into the characteristics and regularity of primary circular reactions. To illustrate the intrinsic characteristic of Li metal batteries (LMBs) in spatial and temporal, it is imperative to employ electron microscopes to characterize the structural components distribution of Li with atomic resolution. This paper summarizes the progress in the characterization and analysis of the interfaces in LMBs with electron microscopes based on the principles of electron-matter interactions. Finally, future trends and the potential of electron microscopes are also discussed to advance our understanding of LMBs.

1. Introduction

Lithium (Li) metal has been hailed the "Holy Grail" anode material for rechargeable high-energy storage systems because of its unparalleled specific capacity (3860 mAh/g) and lowest electrochemical potential (−3.04 V *vs.* the standard hydrogen electrode) [1–3]. However, the large-scale application of Li metal batteries (LMBs) has been hindered by the non-uniform plating/stripping of Li metal, which results in the uncontrolled growth of Li dendrites. Due to the inherent ultrahigh chemical reactivity, Li metal is thermodynamically unstable in all organic electrolytes, which causes a continuous parasitic reaction between Li metal and electrolyte, resulting in the formation of a solid electrolyte interphase (SEI) on Li metal surface [4–7]. The mosaic structure and heterogeneous component SEI lead to inhomogeneous ion diffusion and the growth of Li dendrites. The dendrites on the anode surface with a high degree of curvature are likely to adsorb Li-ions, which aggravate further growth of Li dendrites [8–11]. Unfortunately, Li dendrite growth has the potential to penetrate the separator, leading to internal short circuits, potentially catastrophic combustion and explosion [12–14]. Besides, the mechanical integrity and corresponding passivation functionality of the formed SEI are compromised by the inherent volume variation during the repeated Li plating-stripping cycles, which leads to the generate of "dead Li" [15–17]. These challenges have been identified as the main origins of fast capacity decay and low coulombic efficiency (CE) of LMBs.

To date, great efforts with physical and/or chemical strategies have been developed to solve the abovementioned issue of LMBs [18–21], including but not limited to: (1) Optimizing the composition of the electrolyte to construct a favorable SEI for uniform deposition of Li metal [22–24]; (2) Employing solid-state electrolytes to prevent bursting into flame in case of short-circuits [25–29]; (3) Introducing three-dimensional (3D) current collectors to regulate Li deposition behavior and reduce the Li-ion flux gradient [30–32]; (4) Developing artificial SEI to avoid the direct corrosion from the electrolyte and stabilize the interface between Li metal and electrolyte [33–36]. Although a significant achievement has been made in suppressing Li dendrite growth, the in-depth understanding of Li dendritic growth mechanism remains unclear [13,37-39].

Due to the cycling performance of LMBs mainly depending on the Li deposition behavior characteristics, it is essential to gain a clear understanding of Li dendrites by electron microscope (EM) techniques [40,41]. In general, image resolution is defined as the minimum distance between two points that can be resolved. Up

* Corresponding authors.
E-mail addresses: hdyuan@zjut.edu.cn (H. Yuan), tao@zjut.edu.cn (X. Tao), yujingliu@zjut.edu.cn (Y. Liu).

https://doi.org/10.1016/j.cclet.2023.108812
1001-8417/

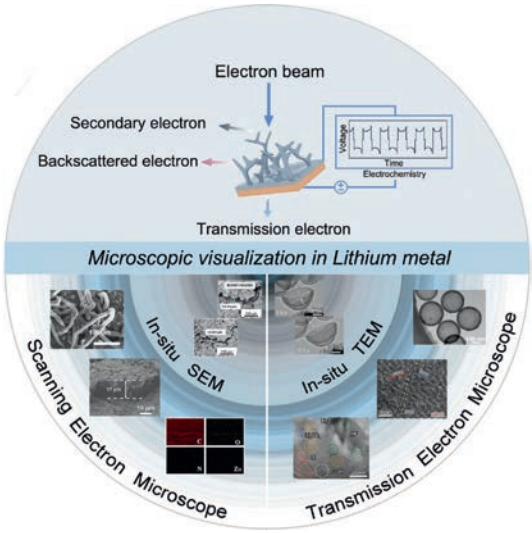

Fig. 1. Schematic illustration of Li dendrites morphology, accumulative dead Li, and the nanostructures of SEI using EMs techniques.

to now, significant advancement has been achieved from optical microscopy with a resolution of 200 nm to EMs with a resolution of 3–200 nm. Therefore, EMs technology have been widely used in the research of LMBs as the most common method for visualizing Li deposition behavior, probing the nanostructure and component of the Li/electrolyte interface in spatial and temporal [42–44]. Specifically, to observe the plated morphology of Li metal during cycling, the *ex-situ* scanning electron microscope (*ex-situ* SEM) technology is typically utilized, which is helpful to understand the deposition behavior of Li metal [35,45-47]. Similarly, synchrotron X-ray tomography imaging with high temporal and spatial resolution provide 3D imaging characterization of rechargeable batteries [48]. Comparing with EM technology, synchrotron X-ray tomography technology can directly characterize the batteries possessing good mechanical stability at a specific electrochemical environment without disassembly, which is made of low X-ray absorbing material that enables X-rays to pass through [48]. Besides, with the aim to clearly study the nanostructure and components of the SEI, *ex-situ* transmission electron microscopy (*ex-situ* TEM) technology is employed to disclose the more detailed with interface [49,50]. Howover, Li metal and the formed SEI are highly sensitive to air, humidity [51], and heat, making it a challenging subject for conventional EMs to accurately analyze their nanostructures and components. In 2017, assisted by the advanced technique of cryogenic TEM (cryo-TEM), the breakthrough in direct observation of sensitive SEI and Li metal at the atomic resolution can be successfully achieved, which is in favor of providing a comprehensive understanding of the failure mechanism in LMBs [52]. Moreover, *in-situ* EM technology enables the direct visualization of the various stages of electrodes during lithiation and delithiation processes, promoting the clear understanding of LMBs in actual condition [53–55]. Specifically, reactive time is a crucial factor which need to be taken into account due to the intrinsic rection speed influences the electrochemical and chemical reactions. Accurate measurements can be achieved when the temporal resolution of the characterization approach is sufficient to monitor the reaction specifics.

In this review, we present a comprehensive summary of recent progress of failure mechanisms of LMBs using various EMs (Fig. 1). We in-depth discuss the representative applications of EMs in LMBs as the following four parts: *ex-situ* SEM technique, *ex-situ* TEM technique, cryo-TEM technique, and *in-situ* EM technique. The structural and chemical characterization of Li/electrolyte interface, Li deposition behavior, and accumulated dead Li are briefly surveyed and studied. Finally, we conclude by presenting our perspective and suggestions on the further development of various EMs in LMBs.

2. *Ex-situ* SEM

Based on the principle of imaging, the contrast of image is defined as comparison of light and dark areas, which determined by the electron production. Surface fluctuations cause the secondary electron yield to increase, resulting in image brightening. Investigating the interface morphological characteristics of Li can provide visual evidence of potential electrochemical performance mechanisms. With the help of secondary electron imaging, the strong three-dimensional sense and depth of field of figure have been exposed to identify the Li deposition behavior on the interface of Li metal [56–59]. Hence, this section will address the research progress using *ex-situ* SEM in Li deposition behavior and the feature of dead Li.

2.1. Li deposition behavior

As one of the most common characterization methods, *ex-situ* SEM has been widely applied to observe the Li deposition behavior. For example, Cui *et al.* analyzed the morphology and distribution of Li nuclei to study the initial stages of nucleation and growth of Li [60]. Illustrated by the SEM images shown in Figs. 2a and b, the size of Li nucleus and nuclear number density are proportional to the inverse ratio and cubic power of overpotential [60], respectively, which is consistent with the classical nucleation and growth theory of Li metal. Based on this result, a strategy to increase the homogeneity and particle density of plated Li was developed *via* utilizing the instantaneous nucleation of Li metal during galvanostatic electrodeposition. In addition, assisted with the help of *ex-situ* SEM, Yang *et al.* clearly provide the insight into the deposition behavior of Li metal on the surface for lithophilic active sites [61]. As shown in Fig. 2c, the Li seeding behavior on the electrode was studied at various current densities ranging from 0.1 mA/cm^2 to 20 mA/cm^2. The highly lithiophilic active sites are present in the thick and uniform Li seed layer, which significantly reduces the Li nucleation barrier, lead to the formation of a uniform Li layer, and inhibit the growth of Li dendrites. Fig. 2d shows that Li existed into the inner space of the 3D SiC/carbon cloth (CC) framework, resulting in the bottom-up deposition process [62]. Hence, current density plays a vital role in the nucleation radius of Li deposition, as well as the morphology and direction of deposition [63].

Introducing Li metal into a host is a promising solution for stabilizing Li metal anode. As shown in Fig. 3a, Wang and coworkers studied the detailed deposition behavior of Li metal within the matrix of 3D Cu foam and Ni-NiO modified 3D Cu foam (3D Ni-NiO) [64]. SEM images show that Li is uniformly plated on the surface of 3D Ni-NiO, which is mainly due to the generation of Li_2ON with high binding affinity in the SEI layer (Fig. 3a). Similarly, lots of inorganic materials such as carbon materials [65,66], fluorides [25], and Li-based alloys [67] with low overpotential have been employed as interface substrates to alleviate nucleation barriers. Li *et al.* developed a 3D lithophilic reduced graphene oxide-based scaffold formulated with abundant N/Zn active sites (ZIF-8@RGO) for loading metallic Li. As shown in Fig. 3b, confirmed by the corresponding energy dispersive spectrometer (EDS) of SEM images, the *in-situ* formation of abundant N/Zn active sites reduced from MOF material (ZIF-8) during cycling can significantly reduce the nucleation overpotential of Li metal, leading to the homogeneous nucleation of Li metal [68]. Fig. 3c exhibits the plating behavior of Li

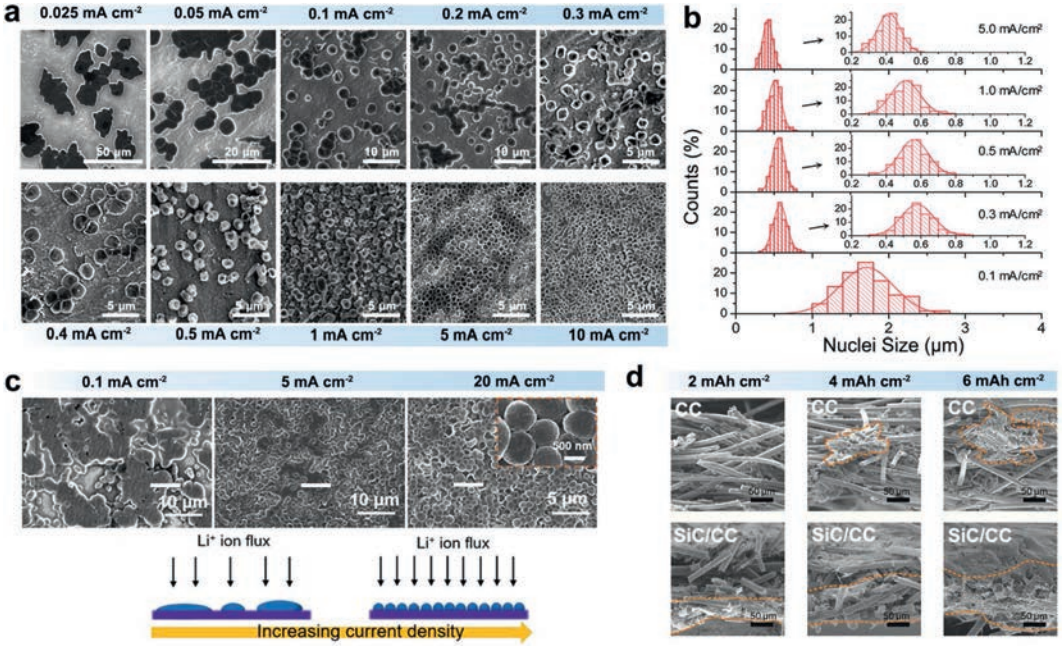

Fig. 2. (a) *Ex-situ* SEM images of Li nuclei deposited at current densities of 0.025–10 mA/cm^2 with areal capacity of 0.1 mAh/cm^2. (b) Distribution diagram of Li particle sizes after 0.025 mAh/cm^2 with current densities of 0.1–5 mA/cm^2. Reproduced with permission [60]. Copyright 2017, American Chemical Society. (c) SEM images of surface morphologies of Li seeds on Cu foil with a plated Li of 0.3 mAh/cm^2 at current densities of 0.1, 5, and 20 mA/cm^2. Reproduced with permission [61]. Copyright 2019, Elsevier. (d) SEM images of the CC and the SiC/CC framework after the deposition of Li metal at the current density of 1 mA/cm^2 with different areal capacities. Reproduced with permission [62]. Copyright 2022, Elsevier.

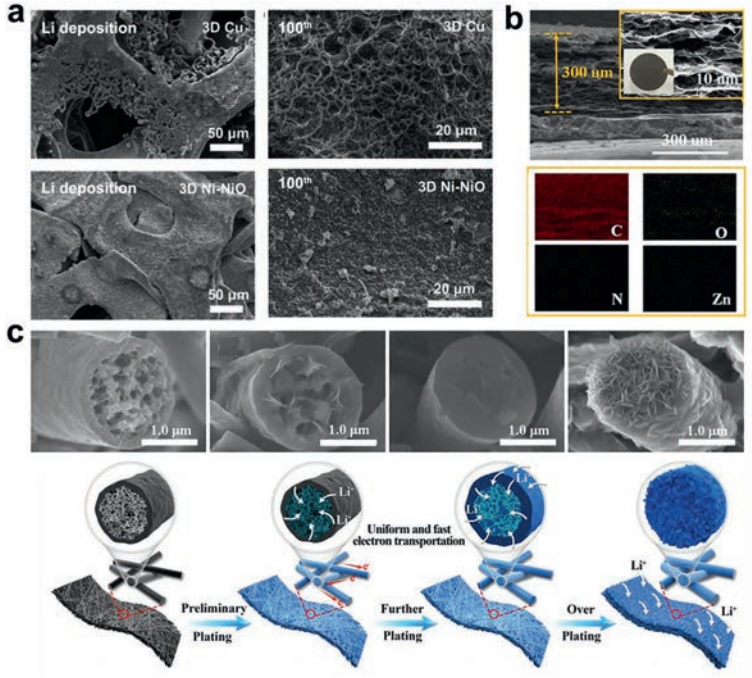

Fig. 3. (a) SEM images of the Li plating behavior on the current collectors of 3D Cu and 3D Ni-NiO. Reproduced with permission [64]. Copyright 2022, Elsevier. (b) SEM images of the obtained ZIF-8@RGO and the corresponding EDS mapping. Reproduced with permission [68]. Copyright 2023, The Royal Society of Chemistry. (c) Schematic illustration and SEM images of the Li plating in the 3D porous core-shell carbon fiber at different states. Reproduced with permission [69]. Copyright 2019, Wiley.

metal within amorphous SiO_2 and TiO_2-modified carbon skeleton. Illustrated from the SEM images, the amorphous SiO_2 and TiO_2 can guide the Li deposition morphology in the 3D porous core-shell carbon fiber during cycling [69]. Significantly, Li was deposited on the outer of the fiber only when the fiber was filled inside, showing the excellent affinity between Li and the modified SiO_2 and TiO_2.

The interfacial feature reveals the uniformity of Li deposition with high resolution, nevertheless, the following problems still need to be continuously studied by interfacial observation: (1) The introduction of lithophilic groups within the Li hosts might aggravate the side reactions occurring at the interface, resulting in poor interface flatness. (2) An excess of insulating lithophilic groups is not conducive to the transfer of electron at the interface, causing

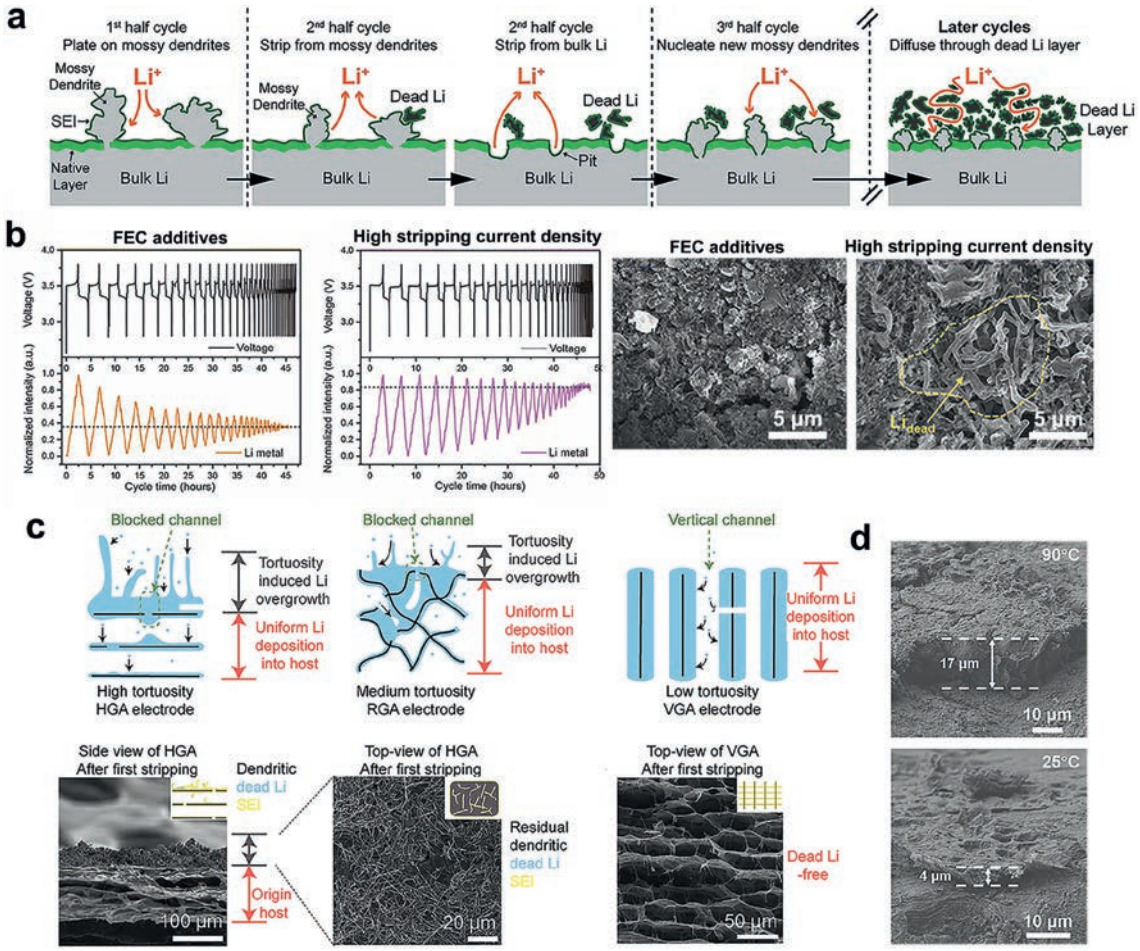

Fig. 4. (a) Schematic illustration of the formation of dead Li. Reproduced with permission [75]. Copyright 2017, The Royal Society of Chemistry. (b) Operando nuclear magnetic resonance (NMR) data under different cycles using FEC as additive, applying high stripping current and SEM images of interface after the cell failure. Reproduced with permission [78]. Copyright 2021, American Association for the Advancement of Science. (c) Schematics of Li deposition in different views after the first Li stripping. Reproduced with permission [79]. Copyright 2020, Elsevier. (d) The morphologies of Li deposition in Li-$LiFePO_4$ batteries using the ET-tolerant electrolyte at 90 °C and 25 °C. Reproduced with permission [80]. Copyright 2020, Wiley.

the growth of Li dendrites. (3) The homogeneity of the distribution of lithophilic groups in porous structures after a long-cycling process should be concerned. In order to further understand the detailed mechanism of the modified lithiophilic groups, the in-depth observation of the interface is needed.

2.2. The feature of dead Li

In view of the surface morphology, the complex three-dimensional structure of Li dendrites was also characterized with the SEM technique. Notably, the plating Li that detached from the electrode surface and fail to participate in the subsequent reaction is referred to as dead Li [70,71]. It is vital to understand the origin of dead Li for avoiding the capacity loss and invalidation of LMBs [72–74]. On the one hand, the Li surface has a lower impedance than the Li bulk, leading to the stripping of Li from the surface and the increasing of impedance. On the other hand, the loss of Li causes the high-volume change, which results in massive Li falling off electrodes, eventually forming an insulating layer composed of dead Li (Fig. 4a) [75–77].

To explore the influence factors for the accumulation of dead Li, Yang and coworkers focused on the electrolyte components and the cycling conditions. As shown in Fig. 4b, fluoroethylene carbonate (FEC) as an additive in the electrolyte exhibits the uniform deposition of Li metal without the accumulation of dead Li during cycling than the cell at higher current density, which is consistent with SEM results [78]. Considering another characteristic measurement, the dead Li is inclined to exist at a higher stripping current density due to the invalidation of SEI. Besides, the formation of dead Li is extremely sensitive to volume change of electrodes. Cui and coworkers focused on the tortuosity in the 3D porous electrode network [79], which affected the properties of ion transport and diffusion. According to the schematic diagram and the corresponding SEM images, the electrode with high-tortuosity (HGA) aggravated the overgrowth of Li dendrites (Fig. 4c), thus increasing the amount of dead Li and seriously reducing the electrode reversibility, while the low tortuosity (VGA) electrode structures was without dead Li [79]. Moreover, environmental factors affect the accumulation of dead Li, such as the high temperature will motivate the adverse reaction between Li and electrolyte, resulting in the inhomogeneous diffusion of Li^+ and the accumulation of dead Li layer. As displayed in Fig. 4d, the thickness of dead Li layer with poor conductivity came up to 17 mm at the high temperature [80]. In contrast, a relatively stable and thin (4 mm) dead Li layer was accumulated on the surface of Li metal when the temperature reduced to 25 °C, indicating that the dead Li layer is induced by high temperature. Clearly, there are numerous factors to cause the accumulation of dead Li, only by intuitively discovering its existence can we take corresponding measures to suppress, thereby the interfacial characterization is indispensable.

3. *Ex-situ* TEM

To obtain more relevant structural information with higher spatial resolution, TEM is used to probe the microscopic nanostructure in LMBs [81,82]. The formation of the transmitted electron images depends on the interaction between the incident electron beam and the sample. When the escape of electrons from the surface of samples, the strength of transmitted electron beam changes due to the effect of the sample for the electron beam. Therefore, the intensity of the electron beam transmitted to the fluorescent screen is non-uniform. Meanwhile, the intensity of the electron image is defined as the contrast, which can be divided into mass contrast and diffraction contrast. The development of TEM observation techniques is profitable to research the internal morphology and crystal structure of materials according to the contrast characteristics in the comprehensive application [83,84].

3.1. Visualization of nanostructure

The theory of mass contrast takes advantage of the difference of sample thickness or atomic number in the sample to make the scattering electron intensity into the aperture of the objective lens and focus on the image plane different, thus forming the contrast of the imaging and promoting research the internal morphology and component distribution of composites [82]. Additionally, the mode of scanning transmission electron microscope (STEM) imaging utilizes the principle of atomic number imaging. The ring detector is used to collect high-angle scattered electrons to form high-angle ring dark field image by means of phase contrast imaging [85]. Rutherford scattering formula points out that the high angle scattering electron intensity is proportional to the square of the atomic number, which facilitates distinguish the atoms of different elements with the high chemical sensitivity [86].

On basis of the mass contrast, the high spatial resolution of TEM was employed to visualize the nanostructure which formed from quantum dot or carbon-based host materials for lithiophilic site. Zhang and coworkers demonstrated the lithophilic chemistry properties of the heteroatom-doped carbons by the first principles calculations and experimental verifications [87]. According to the cluster model calculations and the test of Li nucleation overpotential, the O dopant exhibits excellent lithiophilicity owing to the largest binding energy and the lowest nucleation energy barrier (Figs. 5a and b). Meanwhile, confirmed by the TEM images shown in Fig. 5c, the employed oxygen-containing graphene (OG) can lead to the uniform nucleation, promoting the construction of lithophilic frameworks for LMBs. In comparison to heteroatom-doped carbon materials, the 2D atomic crystal graphdiyne (GDY) as the burgeoning carbon allotrope has a prominent application in suppressing the growth of Li dendrite. Specifically, Li *et al.* found that a large number of uniform copper quantum dots (CuQD) was formed on the surface of polycrystalline copper nanowires (P-CuNW) due to the spontaneous growth of graphdiyne at the crystal boundaries [88]. As shown in Fig. 5d, the growth of CuQD on the surface of GDY has been confirmed by the corresponding TEM images. Meanwhile, the distribution of C element in GDY has also been clearly revealed by the application of EDS (Fig. 5e). The abovementioned results proved that the design and modification of micro/nano structures is a successful strategy to improve interfacial stability, as well as the ion conductivity. For instance, TiO_2@nitrogendoped hollow porous carbon spheres (N–HPCSs) were used as 3D carbon-based host by Wang *et al.*, in which electrode degradation caused by ultrafine TiO_2 seed can promote the fast transfer of ions (Figs. 5f and g) [89]. Notably, metal oxides show high lithiophilic to form alloys and facilitate uniform Li nucleation, such as ZnO [90] and Al_2O_3 [91]. Furthermore, researchers also developed that other hollow structures including Co_3O_4 [92], CuO [93], MnO_2 [94], CuS [95], *etc*., are also beneficial for enhancing the stability of micro/nano interface in LMBs.

3.2. Electrolyte modification

According to the Bragg equation ($2d\sin\theta = n\lambda$), the diffraction comparison of different crystal structures in TEM is beneficial for observing the distribution of components through the cathode electrolyte interface (CEI)/SEI in LMBs. The uncontrollable side reaction between Li metal and electrolyte is the inevitable factor affecting the stability of interfaces in LMBs. Herein, electrolyte modification can be divided into polymer electrolytes [96–98], concentrated electrolytes [99], ionic liquids [100,101], and electrolyte additives [102,103]. In terms of electrolyte modification, TEM technology is the appropriate method for exploring the component of CEI/SEI, regardless of the sample preparation or observation perspective.

In terms of regulating the electrolyte composition, Wang and coworkers proposed a nonaqueous electrolyte by adding aluminum ethoxide ($Al(EtO)_3$) and fluoroethylene carbonate (FEC) as additives to form stable interphase with high conductive [104]. As displayed in Fig. 6a, the CEI layer formed in $Al(EtO)_3$-containing electrolyte (AFE) with higher uniformity can significantly reduce stress-induced cracking and dissatisfactory phase transformation. In addition to interfacial stability, stabilizing electrolytes under low-temperature operations is also the focus of research [105–107]. Guo and coworkers reported the quasi-solid-state polymer electrolyte that could promote the formation of a dual-layered SEI to stabilize the electrolyte interface with an ionic conductivity of 2.2×10^{-4} S/cm at $-20\,^{\circ}C$, effectively suppressing electrolyte oxidation and the dissolution of transition metal (Fig. 6b) [108]. Besides, high-concentration electrolytes (HCEs) [109] and high-concentration electrolytes (LHCEs) [110,111] were also used to improve the compatibility of electrolyte, achieving the efficient LMBs (Fig. 6c). On the basis of the mechanism of electrolyte decomposition, Zhang and coworkers calculated the molecular orbital energy of the obtained additives for building a dense CEI/SEI by density functional theory (DFT) calculation (Fig. 6d) [112]. According to the LUMO energy, the higher reduction potential represents the excellent electron affinity, which is equivalent to react faster with Li and hinder the reduction of solvent.

Ex-situ TEM technology achieves the observation of micro-nano regions, however the following problems still need to be considered in LMBs: (1) Specific information in the amorphous region cannot be detected by TEM, thus it can be used in conjunction with other interfacial characterization measurement. (2) The thickness of samples used in TEM measurement is required, so the application of ultrathin section technology in the samples of LMBs will greatly improve the observing efficiency by the TEM.

4. Cryo-TEM

The high-energy electron beam can greatly improve the resolution of the TEM images, simultaneously the sample would also suffer from heat loss [113,114]. The main reason is that the energy caused by the inelastic collision during the interaction between electrons and matter releases in the form of heat energy, subsequently the heat energy will make the temperature of sample with a low melting point rapidly rise, resulting in thermal decomposition and melt for sample [115]. Due to the drastic heating and irradiation damage, the traditional electronic imaging technology fails in observing the SEI/CEI in LMBs [116]. Therefore, in order to reduce the thermal damage of high-energy electron beams, the cryo-TEM technique has been developed to reduce the melting of

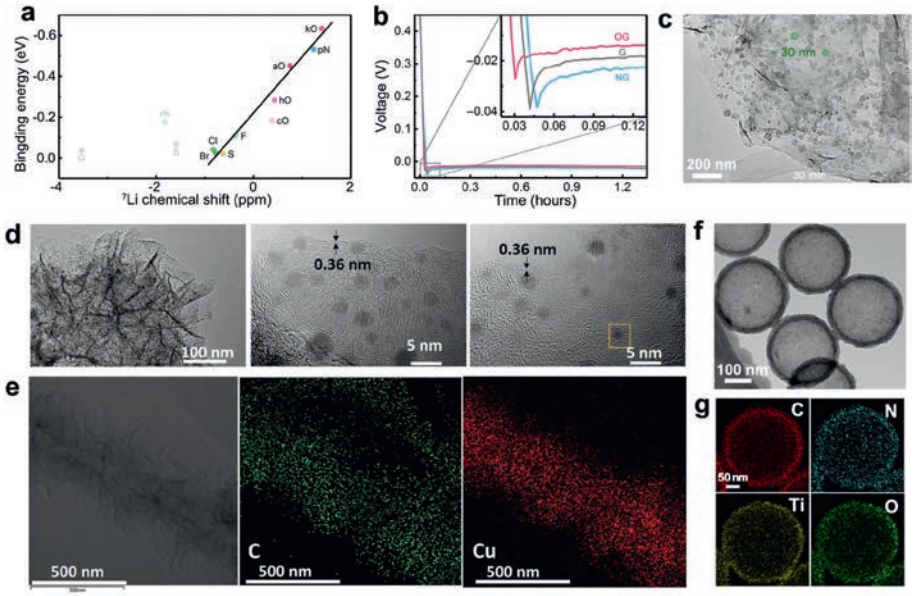

Fig. 5. (a) The proposed principles for designing highly lithophilic Li frameworks with theoretical ^{7}Li chemical shift. (b) Li nucleation characterizations with different electrodes. (c) TEM images of Li deposits using OG electrodes. Reproduced with permission [87]. Copyright 2019, American Association for the Advancement of Science. (d) TEM images of the GDY and HRTEM images of the CuQDs on the GDY nanosheet. (e) Elemental distribution mapping of GDY nanosheet. Reproduced with permission [88]. Copyright 2020, Wiley. (f) TEM image of TiO_2@N–HPCSs. (g) EDS elemental maps of TiO_2@N–HPCSs. Reproduced with permission [89]. Copyright 2022, American Chemical Society.

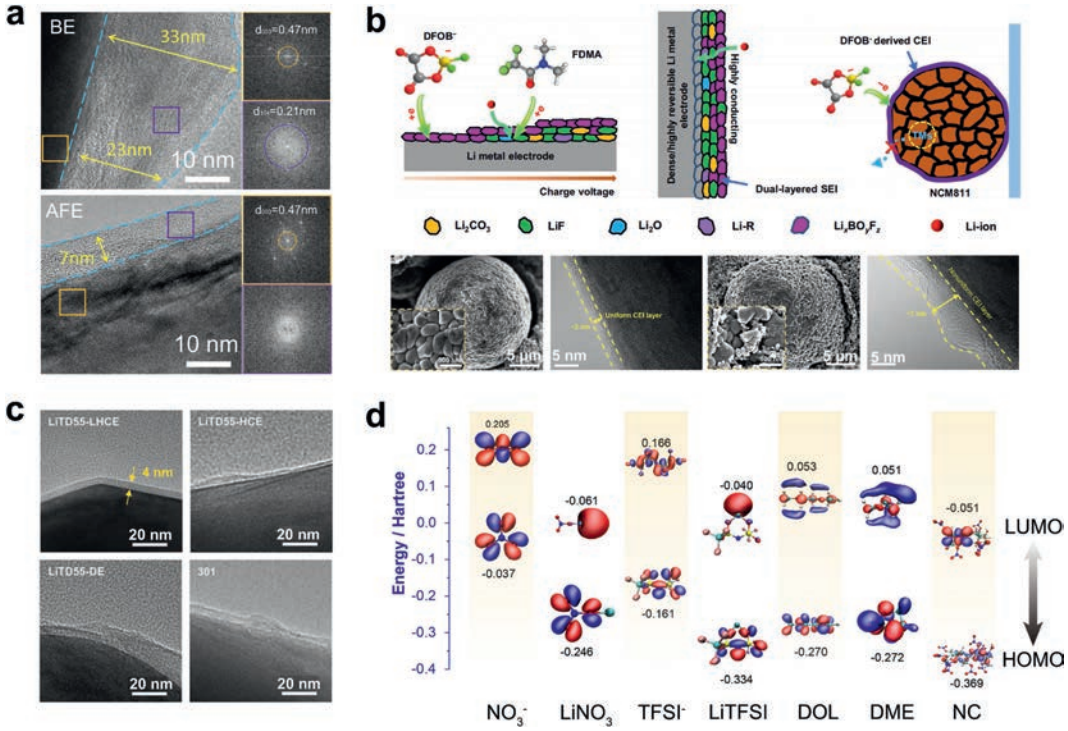

Fig. 6. (a) TEM analyses of the NCM622 particles after 100 cycles in the BE and AFE. Reproduced with permission [104]. Copyright 2022, Nature Publishing Group. (b) Schematic representation and the corresponding TEM images of SEI formed on the Li metal surface (left) and inhibition of the degradation processes in a Li||NCM811 cell (right) using the polymer electrolyte. Reproduced with permission [108]. Copyright 2023, Nature Publishing Group. (c) TEM images of CEI formed in electrolytes with LHCE. Reproduced with permission [110]. Copyright 2023, Elsevier. (d) The highest occupied molecular orbital (HOMO)-lowest unoccupied molecular orbital (LUMO) energy levels of different compositions. Reproduced with permission [112]. Copyright 2021, Wiley.

the sensitive samples, maintaining the integrity of morphology and structure [117].

4.1. Lattice orientation of Li metal

Due to the high sensitivity of Li metal to energy-beam irradiation, it is difficult in detecting the intrinsic lattice orientation of Li metal using the conventional TEM technique. To clarify the lattice orientation of Li metal, Cui *et al.* firstly detected the structure of Li metal and the corresponding SEI with the cryo-TEM technique, revealing the atomic-resolution images of sensitive battery materials in native state (Fig. 7a) [52]. The statistical data indicated that the main growth direction of Li dendrites in carbonate-based electrolyte was ⟨111⟩ (49% by number), the others are ⟨211⟩ (32%)

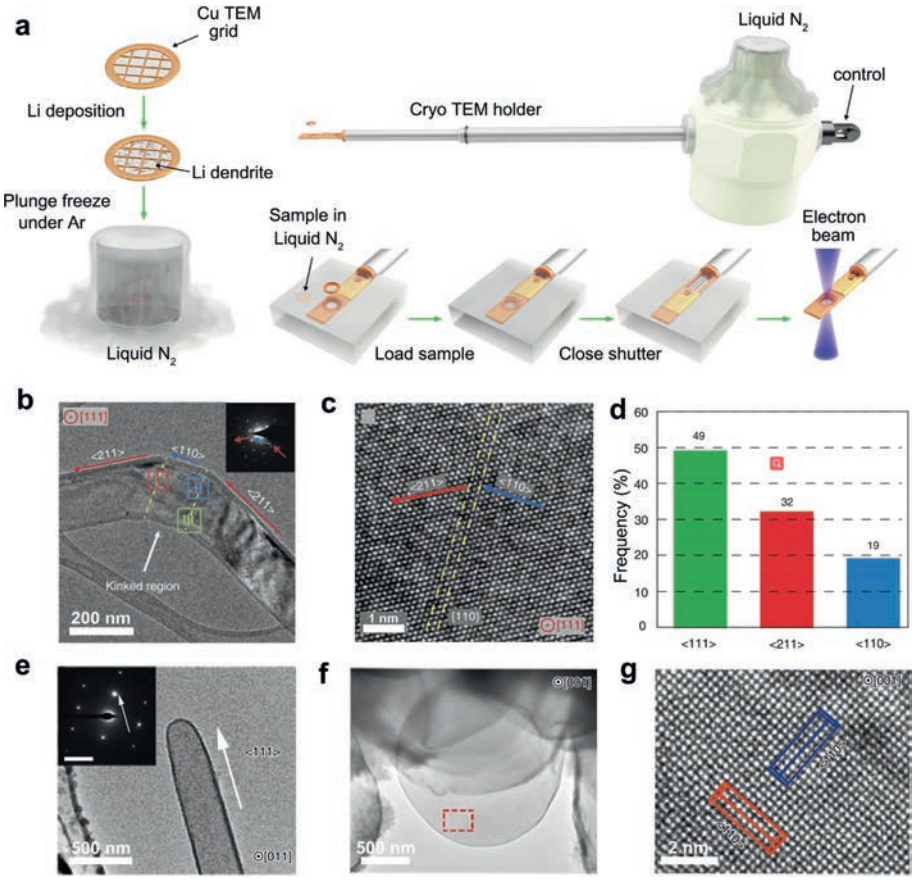

Fig. 7. (a) The transferable process of Li metal by cryo-TEM. (b) TEM image of kinked Li metal dendrite. Inset shows the corresponding SAED pattern. (c) Magnified images of red region I. (d) The frequency with different growth directions of Li dendrites. Reproduced with permission [52]. Copyright 2017, American Association for the Advancement of Science. (e) Cryo-TEM images of the grown Li dendrites without TESM. (f) Cryo-TEM images of the plated Li microspheres with TESM. (g) The corresponding HRTEM images of the marked area along the [001] zone axes. Reproduced with permission [118]. Copyright 2020, Nature Publishing Group.

and ⟨110⟩ (19%), which is consistent with Li surface energies of the broken bond model (Figs. 7b-d). Significantly, Li dendrites became bending growth rather than straight growth of single-crystalline nanowires with the linear direction, while there were no obvious crystal defects in the pathway. Furthermore, Tao *et al.* found that Li microspheres induced by the trifluoroethanol-modified eggshell membrane (TESM) grew preferentially along the ⟨110⟩ and ⟨211⟩ directions, which were also confirmed by the corresponding cryo-TEM results [118], simultaneously the ⟨111⟩ direction was hardly detected. The results showed that the disappearance of the ⟨111⟩ direction of Li with TESM might be strongly related to the growth of Li dendrites, providing an effective view to suppress the dendrite formation with rearrange the surface energy (Figs. 7e-g).

4.2. Identification of SEI/dead Li

In addition to revealing the lattice orientation of Li, the cryo-TEM was also performed to disclose the relationship between the nanostructures of SEI and the electrochemical stability in different electrolytes. Xia *et al.* confirmed the mosaic structure of SEI originated from the electrolyte composing of ethylene carbonate (DC) and diethyl carbonate (DEC) using $LiPF_6$ as Li salt, where the inorganic and organic species including LiF, Li_2O, -COOLi, and ROCOOR randomly distributed in the SEI layer (Fig. 8a) [119]. On the contrary, the SEI layers formed in the ethers-based electrolytes shows a multilayer structure (Fig. 8b), which is consisting of the organic rich inner phase and inorganic rich outer layers with Li_2CO_3 and Li_2O species. Clearly, it is found that carbonate molecules are more likely to react with Li and promote the formation of an organic SEI layer on the surface of Li metal. Based on the understanding of the properties with the corresponding SEI in different electrolytes, the SEI with targeted modification will be succeeded in different characteristics applications, such as fast-charging [120–123], high-voltage [124–126], and high/low temperature [106,127,128]. Besides, the influence of the external environment affects the component of SEI, such as pressure [129,130], moisture [13,131-133], and temperature [50,134,135]. Specifically, Meng *et al.* proposed that uniaxial stack pressure could be used as a powerful tuning knob to precisely tailor the Li deposition morphology and dissolution geometry [129], revealing the composition of SEI at the pressure of 350 kPa (Fig. 8c). Thus, considering the formation of SEI is conducive to the construction of stable interface.

In addition to the component and structure of SEI, the residues of SEI after Li stripping is beneficial for understanding the failed states of batteries during cycling [136]. In general, the SEI breaks due to the volume variation of Li, resulting in the fractured and inactivate Li. Hence, the damaged SEI is the direct trigger for death. Tao *et al.* revealed the morphology and composition of the "dead" SEI and dead Li debris by cryo-TEM [59]. Specifically, the SEI's residues became too feeble to transfer Li^+, trapping the Li in the surrounding region (Fig. 8d). Studied from the high-resolution transmission electron microscope (HRTEM) image and the mass content ratio, Li_2O plays a dominant role in the SEI, isolating metallic Li and incorporating a large amount of Li debris (Figs. 8e and f). Meanwhile, a novel strategy with iodine-redox-chemistry rejuvenated electrochemically inactive Li (Fig. 8g). Particularly, obvious Li debris and dead SEI accumulation were not observed in the SEI nanostructures (Figs. 8h and i).

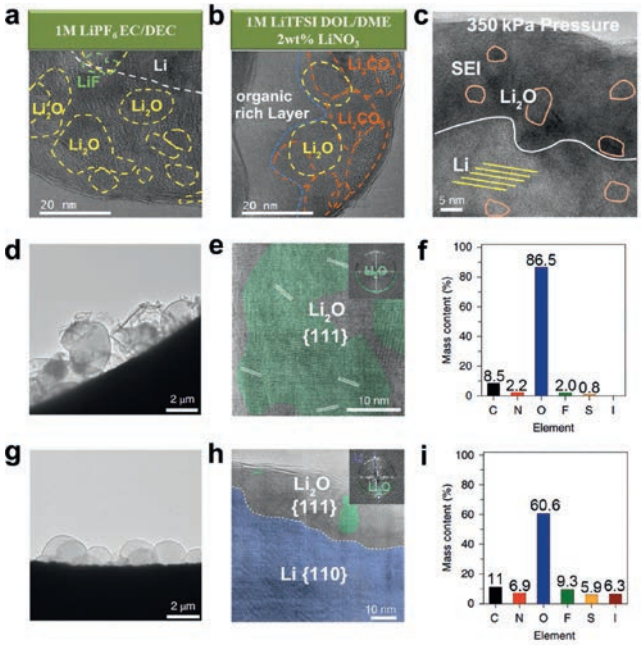

Fig. 8. (a, b) Cryo-TEM images of the SEI layer in the different electrolytes. Reproduced with permission [119]. Copyright 2021, Elsevier. (c) HRTEM images of Li deposited at 350 kPa pressure. Reproduced with permission [129]. Copyright 2021, Nature Publishing Group. (d, e) Cryo-TEM image of the plated Li and SEI in ethers electrolytes. (f) Mass content of the SEI formed in the ethers electrolytes. (g, h) Cryo-TEM image of SEI in ethers electrolytes containing iodine. (i) Mass content of elements in the area from (g). Reproduced with permission [59]. Copyright 2021, Nature Publishing Group.

4.3. Interfacial engineering modification

The high resolution of cryo-TEM provides a possibility to visualize the interfacial engineering modification in LMBs [137]. As shown in Figs. 9a and b, Yuan *et al.* designed an electrolyte-soluble metal fluoride capsule on surface of Cu foil as composite substrates for Li deposition, where the $NaMg(Mn)F_3$ can slowly but constantly release the metallic ions into electrolyte [34]. Due to the higher redox potential of these released metallic ions than Li^+, they will deposit prior to the Li metal and act as a lithiophilic substrate while the F^- is supposed to *in situ* form a LiF-rich SEI layer on the surface of Li anode (Figs. 9c and d), leading to the homogeneous deposition of Li metal. Although the above-mentioned strategy is beneficial for the stability of Li/electrolyte inteface, the lightweight design of LMBs is undoubtedly more suitable for the commercial application. Tao *et al.* proposed self-assembled monolayers (SAMs) with long-range-ordered polar carboxyl groups linked to an aluminum oxide-coated separator to establish strong dipole moments [3], thus leading to the decomposition of LiTFSI and the construction of SEI with enriched LiF nanocrystals within the interface (Fig. 9e). To clarify the degradation kinetics of C-F bond in LiTFSI, the technique of cryo-TEM provides valid evidence in observing a classical mosaic structure of SEI with Li, LiF, LiOH and Li_2O nanocrystal (Figs. 9f and g), which is consistent with DFT and ab initio molecular dynamics (AIMD) calculations.

Besides, it is still hard to obverse the solid-solid interface in LMBs with solid polymer electrolyte (SPE) without the cryo-TEM [138]. Although the SPE and Li metal are heat-sensitive materials, the nanostructure and components of interface between the Li metal and SPE at the atomic level was successfully revealed by the technique of cryo-TEM [25]. Specifically, Sheng *et al.* developed a LiF-enriched interface with the typical mosaic model (Fig. 9h), exhibiting the decomposition of $N(CF_3SO_2)_2^-$ with the addition of Li_2S (Fig. 9i). Similarly, Xin *et al.* used FEC as the additive for polyacrylate-based SPEs to inhibit the interfacial corrosion between Li and SPE [139]. In this work, the formed SEI enriched with disordered/amorphous LiF can significantly stabilize the interface between Li metal and SPE (Figs. 9j and k). The LiF inorganic phase is considered as the ideal interfacial component within the SEI to improve the stability, as well as Li_3N [65,140,141] and Li_2S [142,143].

On the basis of the above research, the feature of cryo-TEM are as follows: (1) The characteristic of the native interface is retained in high-resolution images. (2) It is beneficial to observe the low melting point materials. (3) The atomic arrangement can also be captured even with the damage of electron beams. Hence, the cryo-TEM technique is a promising candidate for observing the unstable interface that raised from the heat-sensitive Li metal, providing more opportunity for the in-depth analysis of LMBs in microscopic visualization research.

5. Real-time observation of Li morphology

Ex-situ observation technique using various EMs is a common method to probe the interfacial properties. In order to confirm the natural state of interface, real-time observation of Li morphology is responsible for revealing the detailed and actual condition. Meanwhile, the electrochemical reactions occur in non-equilibrium states and localization can be detected by the *in-situ* transient electromagnet-electric bias experiments with high spatial and temporal resolution, revealing the dynamic transformation mechanism of electrode materials [144,145]. *In-situ* EM exhibits a direct and real-time view of the lithiation/delithiation process, illustrating the reaction kinetics in electrochemical processes and the structural-performance relationships for LMBs [146,147].

Nowadays, a variety of *in-situ* imaging techniques have been developed to indicate the microstructure transitions and Li^+ diffusion at different scales and temporal resolutions [148,149]. In general, optical microscopy (OM) technique is often used to observe the Li deposition behavior or Li dendrite growth [150–152]. Besides, the transformation of Li stripping/plating processes can be verify with OM observations, showing the inherent correlation between the electrode structure and electrochemical behaviors [153]. Although OM technique can exhibit the failure mechanism of batteries at the macro level, the real-time variation of interface between Li and electrolyte is not fully understood with the intricate characterization [154]. Hence, *in-situ* SEM and TEM techniques reveal the evolution of morphology at the interface, which is conducive to observe the actual interfacial feature [155,156].

5.1. In-situ SEM

To explore the evolution of interface between Li and SPE, Davoisne *et al.* employed the *in-situ* SEM with backscattered electron (BSE) imaging based on the atomic number to certify the differences of β-Li_3PS_4 (LPS) and Li_6PS_5Cl (LPSCl) in cycling performance and failure mechanism [157]. The pre-existing cracks grown at interface of LPS and the uncontrolled growth of Li after the first cycle can be clearly observed in Figs. 10a and b, while LPSCl showed a relatively slow trend. Considering that of the crack feature, the crack in LPS was sharper than that in LPSCl, leading to the fast-growing of Li dendrites. In addition, Li *et al.* elaborated the behavior of Li plating/stripping in all-solid-state batteries using a self-designed *in-situ* probing station to visualize Li dendrites growth and crack propagation (Fig. 10c) [158]. With the increase capacity of Li deposition, the crack of $Li_{6.4}La_3Zr_{1.4}Ta_{0.6}O_{12}$ (LLZTO) became wider gradually. Therefore, due to the influence of stress, Li dendrites pierced into the solid electrolyte through the gap, which were found around the crack zone, resulting in the short

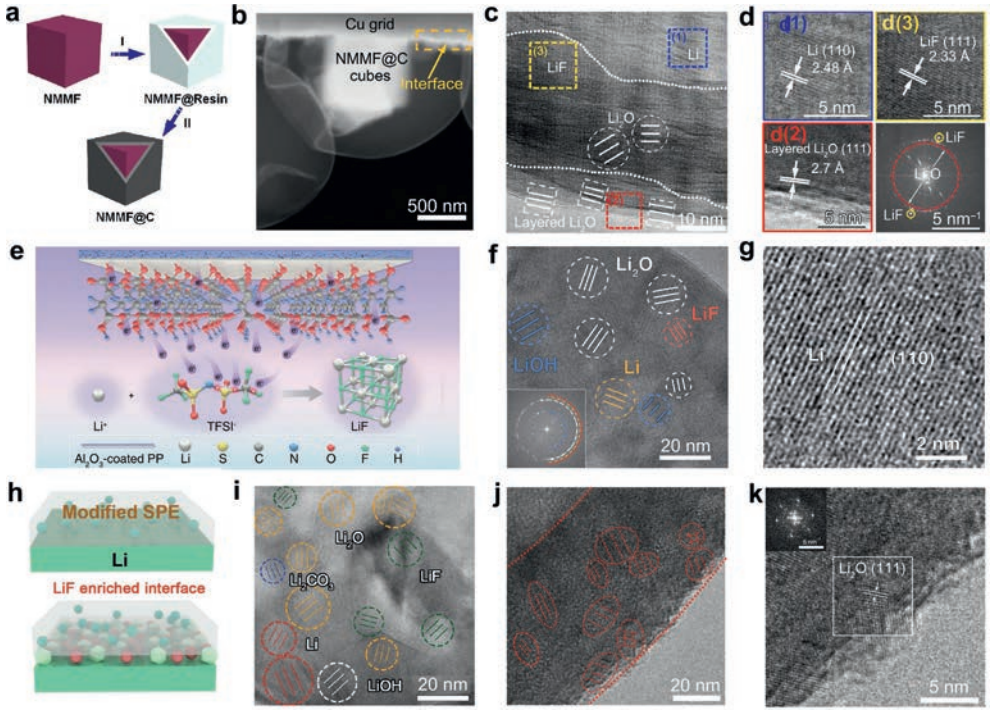

Fig. 9. (a) The fabrication process of the $NaMg(Mn)F_3$@C (NMMF@C) microcubes. (b) Morphology of Li plated with the NMMF@C-modified Cu grid. (c) HRTEM image of the SEI formed on surface of NMMF@C-modified Cu grid. (d) Nanocrystals corresponding to regions (1), (2), and (3) in (c). Reproduced with permission [34]. Copyright 2020, American Association for the Advancement of Science. (e) Schematic illustration of SAMs in LMBs. (f) Enlarged TEM image of the Li/Al_2O_3-$OOC(CH_2)_2COOH$ interface. Inset shows corresponding SAED pattern. (g) HRTEM images of Li nanocrystals. Reproduced with permission [3]. Copyright 2022, American Association for the Advancement of Science. (h) Illustration of the Li/PEO interface. (i) HRTEM image of the interface with Li/PEO. Reproduced with permission [25]. Copyright 2020, Wiley. (j) Cryo-TEM image of the mosaic SEI composed of densely packed nano-sized domains. (k) The atomic structure of a Li_2O nanocrystal inside the SEI. Reproduced with permission [139]. Copyright 2022, Nature Publishing Group.

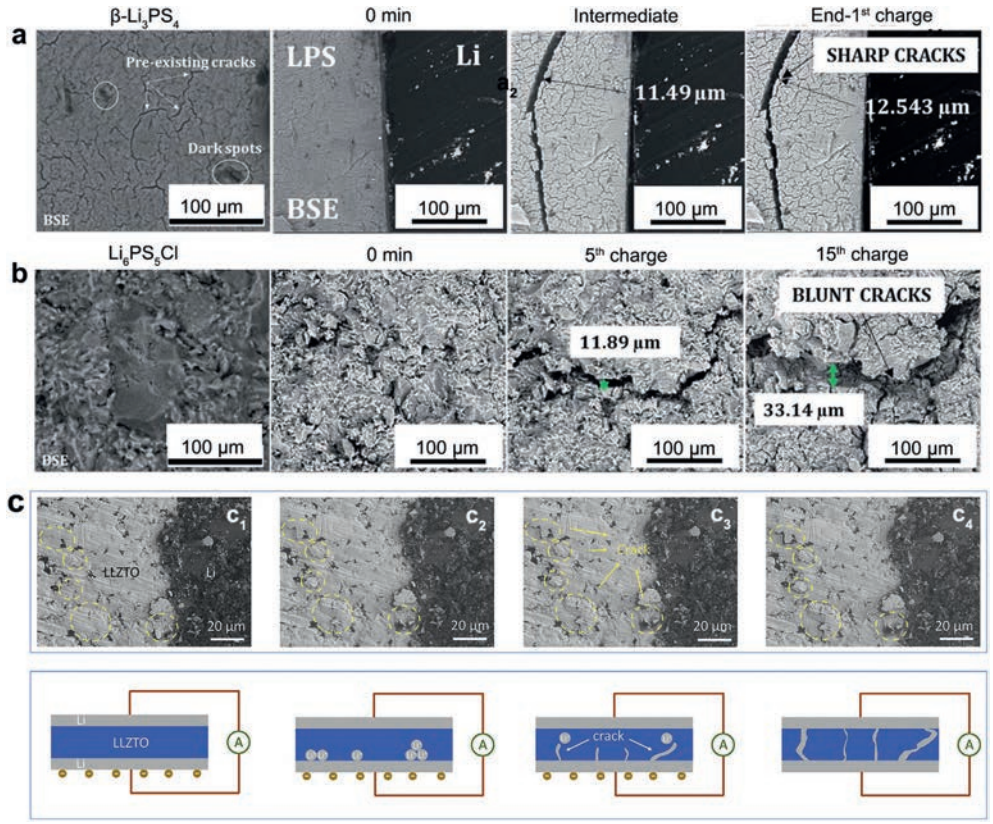

Fig. 10. BSE images of the evolution of (a) β-Li_3PS_4 and (b) Li_6PS_5Cl during cycling. Reproduced with permission [157]. Copyright 2022, The Royal Society of Chemistry. (c) *In-situ* cross-sectional morphology evolution and schematic illustration of LLZTO in the symmetric batteries. Reproduced with permission [158]. Copyright 2019, Elsevier.

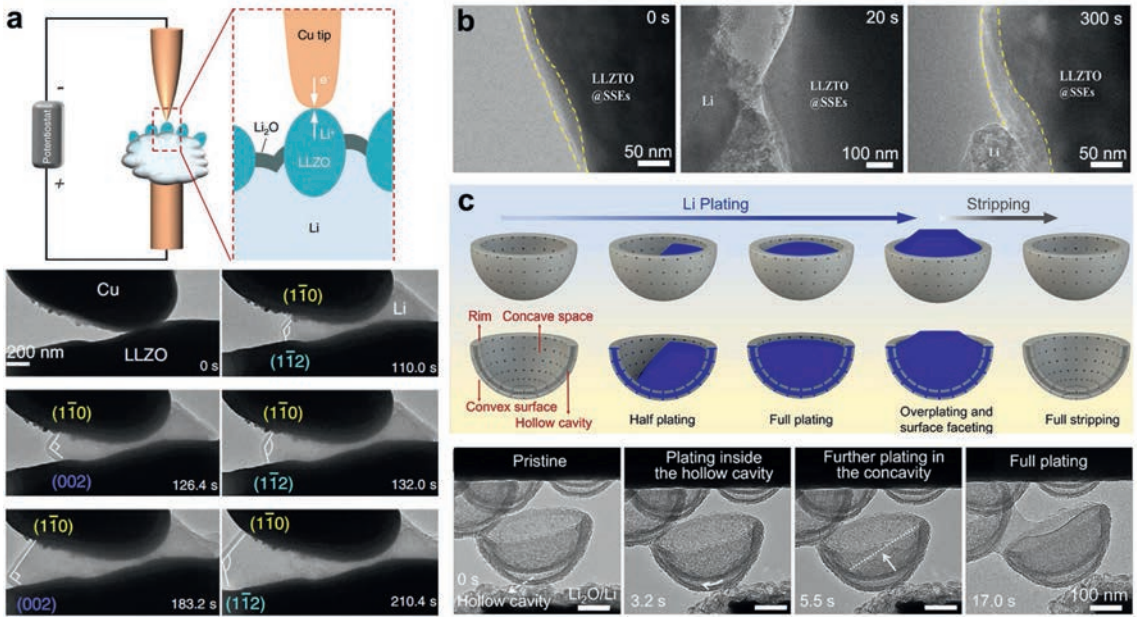

Fig. 11. (a) Schematic of the anode-free Cu|LLZO|Li nanobattery setup for *in-situ* TEM probing. Time-lapsed TEM images revealing the Li growth on the LLZO surface by creeping under a rigid constraint from the Cu current collector. Reproduced with permission [161]. Copyright 2022, Nature Publishing Group. (b) Timelapse *in-situ* TEM images during lithiation. Reproduced with permission [162]. Copyright 2022, Elsevier. (c) Schematic diagrams of Li deposition on a carbon nanobowl. Reproduced with permission [166]. Copyright 2021, American Chemical Society.

circuit in a symmetric Li|LLZTO|Li cell. With the assistance of *in-situ* SEM, the crack growth and failure mechanism at the interface can be successfully illustrated, facilitating the research of real-time morphology and chemical investigation.

5.2. In-situ TEM

In general, polymer and inorganic electrolytes are often used to build batteries, and *in-situ* SEM examination is an efficient way based on the evolution of electrolytes [159,160]. To clarify the mechanism of rate-dependent failure at the interface, the electrochemo-mechanical attack derived from Li is responsible for the invalidation of all-solid-state electrolyte [27,161]. With the help of *in-situ* TEM, Wang *et al.* proposed that the crack initiation at the Li|$Li_7La_3Zr_2O_{12}$ (LLZO) interface is mainly depended on the current density and the efficiency of mass/stress release [161]. With a strong mechanical limit and a low constant bias of 0.2 V, the stress caused by Li deposition generated the single-crystal Li to laterally expand on LLZO (Fig. 11a), while the LLZO particles would crack as stress increased. In addition to visualize the influence of stress at the interface, the intrinsic properties of electrolytes can be intuitively characterized by the *in-situ* observation. Wang *et al.* showed the interface using the LLZTO with good stability rather than rupture after lithiation, leading to the excellent cycling performance in LMBs (Fig. 11b) [162].

In addition to the interfacial studies in solid-state electrolyte, the behavior of Li deposition in carbon spheres is also investigated [163–165]. To reveal the carbon nanospheres with different curvatures and space geometries, Wang *et al.* pointed out that the spatial geometry of carbon nanobowls (CBs) affect the behavior of Li deposition according to their affinity for Li metals (Fig. 11c) [166]. Specifically, CBs with concave and convex surfaces built the enclosed cavity space and semi-enclosed concave space, demonstrating that Li preferentially nucleated and grown on concave surfaces rather than convex ones due to the surface curvature. By means of the observation with *in-situ* TEM, the hollow cavity was filled with Li and subsequently deposited on the concave space, which could be recognized by the volume changes of the hollow cavity. Besides, carbon fibers were proposed as a novel design for the amine functionalization, realizing the reversible and 'self-smoothing' Li deposition [167]. It is an effective measure for building the lithophilic sites to induce Li nucleation, achieving the homogeneous deposition of Li metal during cycling.

There is no doubt that real-time interface can be exposed by *in-situ* observation techniques, while the further studies and innovation need be developed for boosting the interfacial observation technique in LMBs, such as: (1) *In-situ* TEM device can only test for a few cycling, which is unable to realize a long period of real-time testing, thus it can be combined with accelerated testing to develop an efficient *in-situ* TEM technology. (2) The high energy electron beam might induce damage to the interface for *in-situ* observation, resulting in the unveracious interface. Hence, it is necessary to design appropriate reaction environment to avoid heat damage and reveal real-time interface state.

6. Conclusion and outlook

In this review, the application of EM in LMBs have an explicit summary to demonstrate the growth kinetics, micro/nanostructure evolution, and interfacial characteristics of Li metal, which further reveal the failure mechanism of LMBs. It is beneficial to develop a thorough understanding of the nucleation and growth of Li dendrites in light of the principle of interaction between electrons and matter. According to the multi-scale visual observation of Li from micro-order to nano-order, it can provide comprehensive and profound clues to regulate the growth behavior of Li metal. Besides, cryo-TEM possesses the remarkable superiority in reducing the thermal damage for analyzing sensitive battery materials at the sub angstrom resolution, such as the unstable composition and its distribution in SEI. Furthermore, it is worth mentioning that the real-time observation techniques have been utilized as control monitor in revealing the mechanism of dynamic transformation.

Apparently, EM technique plays a crucial role in deepening the cognitive of Li metal, while it still faces challenges and opportunities to exploit a great deal of effective data based on the crystalline lattice in detail. Firstly, the morphology of Li deposition tends to

be spherical when referring to uniformity and stability, while the inherent relationship of the transition from dendrite to globule is still not unknown based on the available literature discussion, it is still one of the difficulties to summarize the transition patterns by electron microscopy. Secondly, amorphous phase is considered as an inevitable presence within the SEI, which originates from electrolyte decomposition, preventing the consumption of active Li. In order to build an effective SEI with great flexibility and performance for long-term cycling, it will be beneficial to investigate the chemical specifics of disordered and amorphous phases. However, the conventional EMs technology fail to analyze the structural characteristics of amorphous phase, it is necessary to combine with other interfacial characterization to explore. Thirdly, it is challenging to make *in-situ* observations of interfacial dynamics, such as the nucleation, growth, and collapse of the Li over time at the atomic scale, because the cryo-state deviates from the conditions that would really be used in practical applications. Furthermore, although TEM observation typically obtains the critical structural information, it is constrained by sample thickness.

Declaration of competing interest

The authors declare that they have no known competing financial interests that could have appeared to influence the work reported in this paper.

Acknowledgments

The authors acknowledge financial support by the National Natural Science Foundation of China (Nos. 51972285, U21A20174, 52171225 and 52102314), the Natural Science Foundation of Zhejiang Province (Nos. LD18E020003 and LQ20E030012), and the Leading Innovative and Entrepreneur Team Introduction Program of Zhejiang (No. 2020R01002).

References

[1] C. Fang, J. Li, M. Zhang, et al., Nature 572 (2019) 511–515.
[2] Z. Zhang, Y. Li, R. Xu, et al., Science 375 (2022) 66–70.
[3] Y. Liu, X. Tao, Y. Wang, et al., Science 375 (2022) 739–745.
[4] Y. Zhu, J. Xie, A. Pei, et al., Nat. Commun. 10 (2019) 2067.
[5] Y. Liu, R. Hu, D. Zhang, et al., Adv. Mater. 33 (2021) e2004711.
[6] G. Wang, C. Chen, Y. Chen, et al., Angew. Chem. Int. Ed. 58 (2019) 1–7.
[7] Y. Liu, Y. Wu, J. Zheng, et al., Nano Energy 82 (2021) 105723.
[8] Y.C. Yin, Q. Wang, J.T. Yang, et al., Nat. Commun. 11 (2020) 1761.
[9] Z.A. Ghazi, Z. Sun, C. Sun, et al., Small 15 (2019) 1900687.
[10] L. Li, S. Basu, Y. Wang, et al., Science 359 (2018) 1513–1516.
[11] M. Ge, X. Zhou, Y. Qin, et al., Chin. Chem. Lett. 33 (2022) 3894–3898.
[12] J. Wang, H. Hu, S. Duan, et al., Adv. Funct. Mater. 32 (2021) 2110468.
[13] X. Shen, Y. Li, T. Qian, et al., Nat. Commun. 10 (2019) 900.
[14] J. Zheng, J. Wang, T. Guo, et al., Small 19 (2023) 2207742.
[15] H. Liu, J. Holoubek, H. Zhou, et al., Energy Storage Mater. 36 (2021) 251–256.
[16] P. Shi, L.P. Hou, C.B. Jin, et al., J. Am. Chem. Soc. 144 (2022) 212–218.
[17] S. Zhang, B. Cheng, Y. Fang, et al., Chin. Chem. Lett. 33 (2022) 3951–3954.
[18] B. Liu, J.G. Zhang, W. Xu, Joule 2 (2018) 833–845.
[19] P. Zhai, T. Wang, H. Jiang, et al., Adv. Mater. 33 (2021) e2006247.
[20] R. Zhang, N.W. Li, X.B. Cheng, et al., Adv. Sci. 4 (2017) 1600445.
[21] B. Zhao, L. Ma, K. Wu, et al., Chin. Chem. Lett. 32 (2021) 125–131.
[22] W. Wu, Y. Liang, D. Li, et al., ACS Nano 16 (2022) 14558–14568.
[23] Z. Piao, R. Gao, Y. Liu, et al., Adv. Mater. 35 (2022) e2206009.
[24] J. Zhang, H. Zhang, L. Deng, et al., Energy Storage Mater. 54 (2023) 450–460.
[25] O. Sheng, J. Zheng, Z. Ju, et al., Adv. Mater. 32 (2020) e2000223.
[26] T. Liu, J. Zheng, H. Hu, et al., J. Energy Chem. 55 (2021) 272–278.
[27] Y. Chen, Z. Wang, X. Li, et al., Nature 578 (2020) 251–255.
[28] M.J. Lee, J. Han, K. Lee, et al., Nature 601 (2022) 217–222.
[29] Z. Shen, J. Zhong, J. Chen, et al., Chin. Chem. Lett. 34 (2023) 107370.
[30] Q. Ke, Q. Xu, X. Lai, et al., Chin. Chem. Lett. 34 (2023) 107602.
[31] T. Zhou, Y. Mu, J. Wu, et al., Chin. Chem. Lett. 33 (2022) 2165–2170.
[32] B. Zhang, H. Shi, Z. Ju, et al., J. Mater. Chem. A 8 (2020) 26045–26054.
[33] S. Li, J. Huang, Y. Cui, et al., Nat. Nanotechnol. 17 (2022) 613–621
[34] H. Yuan, J. Nai, H. Tian, et al., Sci. Adv. 6 (2020) eaaz3112.
[35] Z. Tu, S. Choudhury, M.J. Zachman, et al., Joule 1 (2017) 394–406.
[36] J. Zheng, Z. Ju, B. Zhang, et al., J. Mater. Chem. A 9 (2021) 10251–10259.
[37] C. Zhang, Y. Feng, Z. Han, et al., Adv. Mater. 32 (2020) e1903747.
[38] Y. Wu, N. Liu, Chem 4 (2018) 438–465.
[39] H. Zhang, S. Wang, Y. Wang, et al., Chin. Chem. Lett. 34 (2023) 108031.
[40] Y. Nomura, K. Yamamoto, Adv. Energy Mater. 13 (2023) 2203883.
[41] H. Park, O. Tamwattana, J. Kim, et al., Adv. Energy Mater. 11 (2020) 2003039.
[42] Q. Chen, C. Dwyer, G. Sheng, et al., Adv. Mater. 32 (2020) e1907619.
[43] T. Shang, Y. Wen, D. Xiao, et al., Adv. Energy Mater. 7 (2017) 1700709.
[44] Y. Liu, Z. Ju, B. Zhang, et al., Acc. Chem. Res. 54 (2021) 2088–2099.
[45] S.T. Oyakhire, W. Zhang, Z. Yu, et al., ACS Energy Lett. 8 (2023) 869–877.
[46] Y. Wang, Z. Wang, L. Zhao, et al., Adv. Mater. 33 (2021) e2008133.
[47] P. Zou, Y. Sui, H. Zhan, et al., Chem. Rev. 121 (2021) 5986–6056.
[48] F. Tang, Z. Wu, C. Yang, et al., Small Methods 5 (2021) e2100557.
[49] F. Wu, N. Yao, Nano Energy 11 (2015) 196–210.
[50] A.C. Thenuwara, P.P. Shetty, M.T. McDowell, Nano Lett. 19 (2019) 8664–8672.
[51] M. Yang, Y. Ji, Y. Dong, et al., Chin. Chem. Lett. 34 (2023) 107087.
[52] Y. Li, Y. Li, A. Pei, et al., Science 358 (2017) 506–510.
[53] E. Strelcov, J. Cothren, D. Leonard, et al., Nanoscale 7 (2015) 3022–3027.
[54] I. Issa, C. Gammer, S. Kolitsch, et al., Mater. Today 48 (2021) 29–37.
[55] H. Sun, Q. Liu, J. Chen, et al., ACS Nano 15 (2021) 19070–19079.
[56] Y. Zhao, M. Amirmaleki, Q. Sun, et al., Matter 1 (2019) 1215–1231.
[57] Y. Ma, L. Wei, Y. He, et al., Angew. Chem. Int. Ed. 61 (2022) e202116291.
[58] L. Sheng, Q. Wang, X. Liu, et al., Nat. Commun. 13 (2022) 172.
[59] C. Jin, T. Liu, O. Sheng, et al., Nat. Energy 6 (2021) 378–387.
[60] A. Pei, G. Zheng, F. Shi, et al., Nano Lett. 17 (2017) 1132–1139.
[61] Z. Huang, G. Zhou, W. Lv, et al., Nano Energy 61 (2019) 47–53.
[62] B. Sun, Q. Zhang, W. Xu, et al., Nano Energy 94 (2022) 106937.
[63] J. Xiao, Q. Li, Y. Bi, et al., Nat. Energy 5 (2020) 561–568.
[64] D. Wang, D. Lv, H. Liu, et al., Energy Storage Mater. 49 (2022) 454–462.
[65] S.Y. Kim, K. Kaup, K.H. Park, et al., ACS Mater. Lett. 3 (2021) 930–938.
[66] T. Lyu, F. Luo, D. Wang, et al., Adv. Energy Mater. 12 (2022) 2201493.
[67] D. He, W. Cui, X. Liao, et al., Adv. Sci. 9 (2022) e2105656.
[68] Q. Liu, R. Wang, Z. Liu, et al., J. Mater. Chem. A 11 (2023) 12910–12917.
[69] P. Xue, C. Sun, H. Li, et al., Adv. Sci. 6 (2019) 1900943.
[70] J. Chen, Z. Cheng, Y. Liao, et al., Adv. Energy Mater. 12 (2022) 2201800.
[71] B.S. Vishnugopi, P.P. Mukherjee, Joule 6 (2022) 291–293.
[72] Q. Wang, B. Liu, Y. Shen, et al., Adv. Sci. 8 (2021) e2101111.
[73] J. Liu, Z. Bao, Y. Cui, et al., Nat. Energy 4 (2019) 180–186.
[74] Z. Zhu, Y. Liu, Z. Ju, et al., ACS Appl. Mater. Interfaces 11 (2019) 24205.
[75] K.H. Chen, K.N. Wood, E. Kazyak, et al., J. Mater. Chem. A 5 (2017) 11671–11681.
[76] A. Kushima, K.P. So, C. Su, et al., Nano Energy 32 (2017) 271–279.
[77] Y. Xiang, M. Tao, X. Chen, et al., Nat. Commun. 14 (2023) 177.
[78] Y. Xiang, M. Tao, G. Zhong, et al., Sci. Adv. 7 (2021) eabj3423.
[79] H. Chen, A. Pei, J. Wan, et al., Joule 4 (2020) 938–952.
[80] L.P. Hou, X.Q. Zhang, B.Q. Li, et al., Angew. Chem. Int. Ed. 59 (2020) 15109–15113.
[81] X. Liu, L. Gu, Small Methods 2 (2018) 1800006.
[82] J.C. Yang, M.W. Small, R.V. Grieshaber, et al., Chem. Soc. Rev. 41 (2012) 8179–8194.
[83] S. Liu, X. Ji, J. Yue, et al., J. Am. Chem. Soc. 142 (2020) 2438–2447.
[84] B. Han, D. Feng, S. Li, et al., Nano Lett. 20 (2020) 4029–4037.
[85] S.D. Findlay, R. Huang, R. Ishikawa, et al., Microscopy 66 (2017) 3–14.
[86] Y. Wen, T. Shang, L. Gu, Microscopy 66 (2017) 25–38.
[87] X. Chen, X.R. Chen, T.Z. Hou, et al., Sci. Adv. 5 (2019) eaau7728.
[88] Z. Zuo, F. He, F. Wang, et al., Adv. Mater. 32 (2020) e2004379.
[89] J. Sun, Y. Cheng, H. Zhang, et al., Nano Lett. 22 (2022) 5874–5882.
[90] F. Wang, J. Gao, Y. Liu, et al., J. Mater. Chem. A 10 (2022) 17395–17405.
[91] F. Ren, Z. Li, Y. Zhu, et al., Nano Energy 73 (2020) 104746.
[92] K. Tang, H. Gao, J. Xiao, et al., Chem. Eng. J. 436 (2022) 134698.
[93] L. Gao, C. Sun, D. Zhang, et al., Chem. Eng. J. 451 (2023) 138410.
[94] Y. Fan, H. Li, X. He, et al., ACS Appl. Energy Mater. 5 (2022) 10034–10044.
[95] Y. Chen, J. Li, Z. Lei, et al., Adv. Energy Mater. 10 (2020) 1903401.
[96] Q. Ma, S. Fu, A.J. Wu, et al., Adv. Energy Mater. 13 (2023) 2203892.
[97] C. Fu, G. Homann, R. Grissa, et al., Adv. Energy Mater. 12 (2022) 2200412.
[98] Z. Chu, S. Zhuang, J. Lu, et al., Chin. Chem. Lett. 34 (2023) 107563.
[99] S. Wang, Z. Xue, F. Chu, et al., J. Energy Chem. 79 (2023) 201–210.
[100] W.J. Cho, S.K. Cho, J.H. Lee, et al., J. Mater. Chem. A 11 (2023) 1676–1683.
[101] U. Pal, D. Rakov, B. Lu, et al., Energy Environ. Sci. 15 (2022) 1907–1919.
[102] D. Zhang, M. Liu, J. Ma, et al., Nat. Commun. 13 (2022) 6966.
[103] G. Jiang, J. Liu, J. He, et al., Adv. Funct. Mater. 33 (2023) 2214422.
[104] Y. Zhang, Y. Wu, H. Li, et al., Nat. Commun. 13 (2022) 1297.
[105] Y. He, P. Zou, S.M. Bak, et al., ACS Energy Lett. 7 (2022) 2866–2875.
[106] A. Hu, F. Li, W. Chen, et al., Adv. Energy Mater. 12 (2022) 2202432.
[107] N. Sun, R. Li, Y. Zhao, et al., Adv. Energy Mater. 12 (2022) 2200621.
[108] Z. Li, R. Yu, S. Weng, et al., Nat. Commun. 14 (2023) 482.
[109] C. Zhang, S. Gu, D. Zhang, et al., Energy Storage Mater. 52 (2022) 355–364.
[110] J. Li, H. Hua, X. Deng, et al., Chem. Eng. J. 452 (2023) 139398.
[111] Z. Lin, Y. Wang, Y. Li, et al., Energy Storage Mater. 53 (2022) 917–926.
[112] Y. Luo, T. Li, H. Zhang, et al., Angew. Chem. Int. Ed. 60 (2021) 11718–11724.
[113] J. Wang, J. Zhang, S. Cheng, et al., Nano Lett. 21 (2021) 3245–3253.
[114] Y. Liu, D. Lin, Y. Li, et al., Nat. Commun. 9 (2018) 3656.
[115] X. Wang, G. Pawar, Y. Li, et al., Nat. Mater. 19 (2020) 1339–1345.
[116] X. Gao, Y.N. Zhou, D. Han, et al., Joule 4 (2020) 1864–1879.
[117] X. Cao, X. Ren, L. Zou, et al., Nat. Energy 4 (2019) 796–805.
[118] Z. Ju, J. Nai, Y. Wang, et al., Nat. Commun. 11 (2020) 488.
[119] S. Yuan, S. Weng, F. Wang, et al., Nano Energy 83 (2021) 105847.
[120] Z. Wu, C. Wang, Z. Hui, et al., Nat. Energy 8 (2023) 340–350.
[121] G. Zhang, J. Chang, L. Wang, et al., Nat. Commun. 14 (2023) 1081.

[122] J.G. Zhang, W. Xu, J. Xiao, et al., Chem. Rev. 120 (2020) 13312–13348.
[123] X. Han, T. Wu, L. Gu, et al., Chin. Chem. Lett. 34 (2023) 107594.
[124] P. Xiao, Y. Zhao, Z. Piao, et al., Energy Environ. Sci. 15 (2022) 2435.
[125] L. Lin, K. Qin, Y.S. Hu, et al., Adv. Mater. 34 (2022) e2110323.
[126] S.J. Tan, J. Yue, X.C. Hu, et al., Angew. Chem. Int. Ed. 58 (2019) 7802–7807.
[127] J. Holoubek, H. Liu, Z. Wu, et al., Nat. Energy 2026 (2021) 303–313.
[128] P. Xiao, R. Luo, Z. Piao, et al., ACS Energy Lett. 6 (2021) 3170.
[129] C. Fang, B. Lu, G. Pawar, et al., Nat. Energy 6 (2021) 987–994.
[130] W. Zhang, X. Yang, J. Wang, et al., Small 19 (2023) 2207540.
[131] K. Liao, S. Wu, X. Mu, et al., Adv. Mater. 30 (2018) e1705711.
[132] Y. Xiao, R. Xu, C. Yan, et al., Sci. Bull. 65 (2020) 909–916.
[133] Y. Zhang, W. Lv, Z. Huang, et al., Sci. Bull. 64 (2019) 910–917.
[134] J. Wang, W. Huang, A. Pei, et al., Nat. Energy 4 (2019) 664–670.
[135] T. Waldmann, M. Wilka, M. Kasper, et al., J. Power Sources 262 (2014) 129–135.
[136] M. Tao, Y. Xiang, D. Zhao, et al., Nano Lett. 22 (2022) 6775–6781.
[137] O. Sheng, C. Jin, M. Chen, et al., J. Mater. Chem. A 8 (2020) 13541.
[138] Q. Yu, K. Jiang, C. Yu, et al., Chin. Chem. Lett. 32 (2021) 2659–2678.
[139] R. Lin, Y. He, C. Wang, et al., Nat. Nanotechnol. 17 (2022) 768–776.
[140] C. Lu, M. Tian, X. Zheng, et al., Chem. Eng. J. 430 (2022) 132722.
[141] S. Ye, L. Wang, F. Liu, et al., Adv. Energy Mater. 10 (2020) 2002647.
[142] S. Luo, X. Liu, X. Zhang, et al., ACS Energy Lett. 7 (2022) 3064–3071.
[143] F. Liu, L. Wang, Z. Zhang, et al., Adv. Funct. Mater. 30 (2020) 2001607.
[144] J. Woods, N. Bhattarai, P. Chapagain, et al., Nano Energy 56 (2019) 619–640.
[145] J. Lu, T. Wu, K. Amine, Nat. Energy 2 (2017) 17011.
[146] Y. Yuan, K. Amine, J. Lu, et al., Nat. Commun. 8 (2017) 15086.
[147] E.R. Adkins, T. Jiang, L. Luo, et al., ACS Energy Lett. 3 (2018) 2829–2834.
[148] Z. Xie, Z. Jiang, X. Zhang, J. Am. Chem. Soc. 164 (2017) A2110–A2123.
[149] J. Cui, H. Zheng, K. He, Adv. Mater. 33 (2021) e2000699.
[150] Y. Shi, J. Wan, G.X. Liu, et al., Angew. Chem. Int. Ed. 59 (2020) 18120–18125.
[151] T. Chen, F. Meng, Z. Zhang, et al., Nano Energy 76 (2020) 105068.
[152] Q. Zhao, Z. Tu, S. Wei, et al., Angew. Chem. Int. Ed. 57 (2018) 992–996.
[153] P. Qing, Z. Wu, A. Wang, et al., Adv. Mater. 35 (2023) e2211203.
[154] Y. Luo, T. Li, H. Zhang, et al., J. Energy Chem. 56 (2021) 14–22.
[155] M. Golozar, A. Paolella, H. Demers, et al., Commun. Chem. 2 (2019) 131.
[156] X. Liu, R.G. Mendez, A.R. Lupini, et al., Nat. Mater. 20 (2021) 1485–1490.
[157] N.G. Yadav, N. Folastre, M. Bolmont, et al., J. Mater. Chem. A 10 (2022) 17142–17155.
[158] Q. Li, T. Yi, X. Wang, et al., Nano Energy 63 (2019) 103895.
[159] H. Yang, P. Tang, N. Piao, et al., Mater. Today 57 (2022) 279–294.
[160] S. Kaboli, H. Demers, A. Paolella, et al., Nano Lett. 20 (2020) 1607–1613.
[161] H. Gao, X. Ai, H. Wang, et al., Nat. Commun. 13 (2022) 5050.
[162] J. Li, Y. Cai, Y. Cui, et al., Nano Energy 95 (2022) 107027.
[163] G. Zheng, S.W. Lee, Z. Liang, et al., Nat. Nanotechnol. 9 (2014) 618–623.
[164] D. Lin, Y. Liu, Z. Liang, et al., Nat. Nanotechnol. 11 (2016) 626–632.
[165] H. Wang, Y. Li, Y. Li, et al., Nano Lett. 19 (2019) 1326–1335.
[166] W. Ye, L. Wang, Y. Yin, et al., ACS Energy Lett. 6 (2021) 2145–2152.
[167] C. Niu, H. Pan, W. Xu, et al., Nat. Nanotechnol. 14 (2019) 594–601.